The Astrophysical Journal, 893:135 (16pp), 2020 April 20 https://doi.org/10.3847/1538-4357/ab7a14
© 2020. The American Astronomical Society. All rights reserved.

Mass Functions of Giant Molecular Clouds and Young Star Clusters in Six Nearby Galaxies

Angus Mok[1], Rupali Chandar[1], and S. Michael Fall[2]
[1] Department of Physics & Astronomy, The University of Toledo, Toledo, OH 43606, USA; mok.angus@gmail.com
[2] Space Telescope Science Institute, Baltimore, MD 21218, USA
Received 2019 October 28; revised 2020 February 21; accepted 2020 February 24; published 2020 April 23

Abstract

We compare the mass functions of young star clusters (ages $\leqslant 10$ Myr) and giant molecular clouds (GMCs) in six galaxies that cover a large range in mass, metallicity, and star formation rate (LMC, M83, M51, NGC 3627, the Antennae, and NGC 3256). We perform maximum-likelihood fits of the Schechter function, $\psi(M) = dN/dM \propto M^{\beta}\exp(-M/M_{*})$, to both populations. We find that most of the GMC and cluster mass functions in our sample are consistent with a pure power-law distribution ($M_{*} \rightarrow \infty$). M51 is the only galaxy that shows some evidence for an upper cutoff (M_{*}) in both populations. Therefore, physical upper mass cutoffs in populations of both GMCs and clusters may be the exception rather than the rule. When we perform power-law fits, we find a relatively small range of indices $\beta_{\rm PL} = -2.3 \pm 0.3$ for our GMC sample and $\beta_{\rm PL} = -2.0 \pm 0.3$ for the cluster sample. This result, that $\beta_{\rm Clusters} \approx \beta_{\rm GMC} \approx -2$, is consistent with theoretical predictions for cluster formation and suggests that the star formation efficiency is largely independent of mass in the GMCs.

Unified Astronomy Thesaurus concepts: Star formation (1569); Young star clusters (1833); Giant molecular clouds (653)

1. Introduction

A comparison of the mass functions of giant molecular clouds (GMCs) and young stellar clusters (with ages $\tau \lesssim 10$ Myr) in nearby galaxies provides important clues to the star formation process. Clusters form in the densest parts, the clumps, within GMCs (see Krumholz et al. 2019 for a recent review). Even as they form, clusters begin to lose mass through feedback from massive stars. This feedback eventually removes the remaining gas, thereby limiting the star formation efficiency (SFE) and setting the shape of the cluster mass function. In a first approximation, the mass functions of both GMCs and clusters can be described by a simple power law, $\psi(M) = dN/dM \propto M^{\beta}$. Some recent works suggest that these mass functions may have a truncation or downturn at the upper end. This can be represented by a Schechter (1976) function, $\psi(M) \propto M^{\beta}\exp(-M/M_{*})$, i.e., a power law with an exponential cutoff at M_{*}.

It is important to distinguish here between *statistical* and *physical* cutoffs in the mass function. All samples have an apparent or statistical upper "cutoff," simply because they run out of objects (GMCs or clusters). In the case of a pure power law with $\beta \approx -2$, this maximum cluster mass is expected to scale approximately linearly with the total number of objects due to sampling statistics, so that galaxies with more GMCs and clusters have higher apparent cutoff masses than galaxies with fewer GMCs and clusters. To date, published cutoff masses for cluster populations are largely consistent with this expected size-of-sample effect (e.g., Mok et al. 2019). In this work, we assess whether or not the data show a physical, i.e., an exponential-like, downturn at the upper end of the mass function that is not simply the result of sampling statistics.

It is well established that the mass functions of young star clusters have $\beta \approx -2.0 \pm 0.2$ (e.g., Zhang & Fall 1999; Fall & Chandar 2012; Chandar et al. 2017; Krumholz et al. 2019). Currently, the shapes of the mass functions of GMCs are less well determined, but theory and simulations suggest they should also have $\beta \approx -2$. (e.g., Elmegreen & Falgarone 1996; Fleck 1996; Wada et al. 2000; Guszejnov et al. 2018). Observational work on GMC populations in nearby galaxies has found values of β ranging from -1.5 in the inner Milky Way disk to -2.9 in M33 (Rosolowsky 2005), with results for other galaxies somewhere between these two extremes (e.g., Blitz et al. 2007). At least part of the reason for the large variation in published results is likely the use of different fitting methods, observational techniques, mass ranges studied, selection criteria, and other assumptions made in the analysis. More recent observational results have found a smaller range of β for populations of GMCs in those same galaxies, with values such as -1.8 in the inner Milky Way (Rice et al. 2016) and -2.0 in M33 (Gratier et al. 2012). However, it remains unclear if the power-law index β for the observed mass functions of GMCs varies significantly among galaxies, or if there is a near-universal value (as found for cluster populations). Another open question is whether GMC mass functions are flatter, steeper, or similar to those of the young clusters that form in the same galaxy.

It also remains uncertain whether the upper cutoffs in the mass functions of young clusters and GMCs are predominantly statistical or physical. For *cluster* populations, cutoffs have been claimed in NGC 4041 (Konstantopoulos et al. 2013), M83 (Bastian et al. 2012; Adamo et al. 2015), M31 (Johnson et al. 2017), M51 (Messa et al. 2018b), and the Antennae (Jordán et al. 2007). On the other hand, Mok et al. (2019) applied a uniform maximum-likelihood fitting procedure to a sample of young clusters in eight nearby galaxies, including M83, M51, and the Antennae, and found that the majority of the galaxies do not show evidence for a physical cutoff, but are consistent with the expectations of a statistical cutoff. Whitmore et al. (2020) reached a similar conclusion about physical cutoffs for clusters in NGC 4449, as did Cook et al. (2019) for a composite of 17 dwarf galaxies studied as part of the LEGUS project. For GMC populations, evidence of a cutoff M_{*} at the $>3\sigma$ level has been claimed for some galaxies

(e.g., M33, Rosolowsky et al. 2007; NGC 4256, Utomo et al. 2015), with weak (2–3σ) evidence (e.g., M51, Colombo et al. 2014; NGC 300, Faesi et al. 2018; NGC 6946, Wu et al. 2017), or no evidence found in others (e.g., in outer disk of the Milky Way, Rice et al. 2016; the LMC Wong et al. 2011). One of the main goals of this work is to use the same fitting method for GMC and cluster samples. We will use a uniform procedure for both populations to establish their relation to one another and determine any galaxy-to-galaxy variations.

The relation between the shapes of the GMC and cluster mass functions is dictated by early stellar feedback mechanisms. Fall et al. (2010, hereafter FKM), analytically derived simple relations between the power-law indicies of gas-dominated protoclusters and the resulting stellar clusters in the limiting cases of energy- and momentum-driven feedback, which correspond to the minimum and maximum radiative losses inside protoclusters (clumps and GMCs). These relations in turn depend on the relation between the radii and masses of the protoclusters, $R_h \propto M^{\alpha}$. Observations in the Milky Way and LMC indicate $\alpha \approx 0.5$, i.e., roughly constant mean surface density, for both GMCs (Larson 1981; Blitz et al. 2007) and clumps (FKM; Wu et al. 2010; Wong et al. 2019). For $\alpha \approx 0.5$ and typical values of $\beta_{\rm GMC} \approx -2$, the FKM model predicts $\beta_{\rm GMC} \approx \beta_{\rm Clusters} \approx -2$. This is because the SFE is independent of the initial masses of the protoclusters and dependent mainly on their surface density (Σ). Recent hydrodynamical simulations of star formation inside molecular clouds of various masses agree with the predicted SFE from this analytical model (e.g., Grudić et al. 2018; Kim et al. 2018).

It has also been suggested that the SFE can be measured using the ratio between the upper mass cutoff or truncation mass M_* in the GMC and cluster populations (e.g., Gieles et al. 2006; Kruijssen 2014). This method has been recently applied in M51, with $M_{*,\rm Clusters}/M_{*,\rm GMC}$ estimated to be $\sim$1% (Messa et al. 2018a). However, this method is only appropriate in cases where a physical (not just a statistical) cutoff is detected with high confidence in both populations.

In this work, we uniformly apply the robust maximum-likelihood fitting method developed in Mok et al. (2019) to the GMC and cluster populations in six nearby galaxies (LMC, M83, M51, NGC 3627, the Antennae, and NGC 3256), selected to have high-quality catalogs for both populations. The galaxies span a wide range in mass, morphology, and star formation rate (SFR). The rest of this paper is organized as follows. In Section 2, we present the GMC catalogs and their mass functions. In Section 3, we present the cluster catalogs and their mass functions, including a new catalog for NGC 3627. In Section 4, we present the results of maximum-likelihood fits of a Schechter function and power law to the cluster and GMC masses. In Sections 5 and 6, we discuss and summarize the main implications of our results.

2. GMCs

In this section, we present catalogs of the GMCs in our six target galaxies. Ground-based optical images of each galaxy are shown in Figure 1. Some basic properties of the galaxies, such as their distance and SFR, are summarized in Table 1. Four out of six of our galaxies have published GMC catalogs (LMC, M83, M51, and the Antennae), which we summarize in Section 2.1. We present new GMC catalogs for NGC 3627 and NGC 3256 based on archival Atacama Large Millimeter/submillimeter Array (ALMA) observations in Section 2.2. The coverage for the molecular gas surveys is also shown in Figure 1 and overlaps significantly with the available cluster catalogs. Important details about the observations, such as the observed CO transition and the beam size (in arcsec and parsecs), are listed in Table 2.

2.1. Previous Catalogs

Below, we summarize some basic information about the published GMC catalogs in the LMC, M83, M51, and the Antennae:

1. *LMC:* A catalog of 543 GMCs was published by Wong et al. (2011), based on CO(1–0) observations taken with the ATNF Mopra Telescope. They assume a value for the CO-to-H_2 ($\alpha_{\rm CO}$) conversion factor of 4.8 $M_\odot$ (K km s^{-1} pc^2)$^{-1}$. The coverage is quite piecemeal, and the proximity of the LMC gives this catalog significantly higher physical resolution compared with the others in our sample.
2. *M83:* A catalog of 873 GMCs was published by Freeman et al. (2017), based on ALMA CO(1–0) observations from project 2012.1.00762.S (PI: A. Hirota). They assume an $\alpha_{\rm CO}$ value of 4.35 $M_\odot$ (K km s^{-1} pc^2)$^{-1}$. The catalog covers the nuclear starburst and parts of the northern region.
3. *M51:* A catalog of 1507 GMCs was published by Colombo et al. (2014), based on IRAM CO(1–0) observations taken as part of the PAWS survey (Schinnerer et al. 2013). They assume a value for $\alpha_{\rm CO}$ of 4.4 $M_\odot$ (K km s^{-1} pc^2)$^{-1}$. The survey covers the center and both inner spiral arms of the galaxy, but not the outer arms.
4. *Antennae:* A catalog of 142 GMCs was published by Zaragoza-Cardiel et al. (2014), based on ALMA CO(3–2) observations from the ALMA science verification program and project 2011.0.00876.S (PI: B. Whitmore). They assume a value for the CO-to-H_2 ($\alpha_{\rm CO}$) conversion factor of 4.8 $M_\odot$ (K km s^{-1} pc^2)$^{-1}$, and a line ratio between CO(3–2) and CO(1–0) of 1.8. Coverage is restricted mostly to the overlap region and both nuclei of this merging system.

From the published Colombo et al. (2014) catalog, the mean uncertainty in the flux measurements of GMCs in M51 (above the adopted completeness limit) is close to $\sim$0.3 dex. We will adopt this as a fiducial value for the errors in the GMC masses.

2.2. New Catalogs

We produce new catalogs of GMCs for NGC 3627 and NGC 3256, since no published catalogs currently exist for these galaxies. After downloading the pipeline calibrated data sets for NGC 3627 (project 2015.1.00956.S, PI: A. Leroy) and NGC 3256 (project 2015.1.00714.S, PI: K. Silwa) from the ALMA archive, we perform our data reduction and imaging using the CASA software package (McMullin et al. 2007). We first perform continuum subtraction for the individual interferometric data sets and then combine the results from the 12 and 7 m (ACA) arrays for each galaxy. To image the data set, we use the noninteractive cleaning process in the TCLEAN routine. We select the area of interest in the two galaxies, using the line-free regions in the datacube to estimate the noise, and then run the TCLEAN process until it reaches a clean threshold

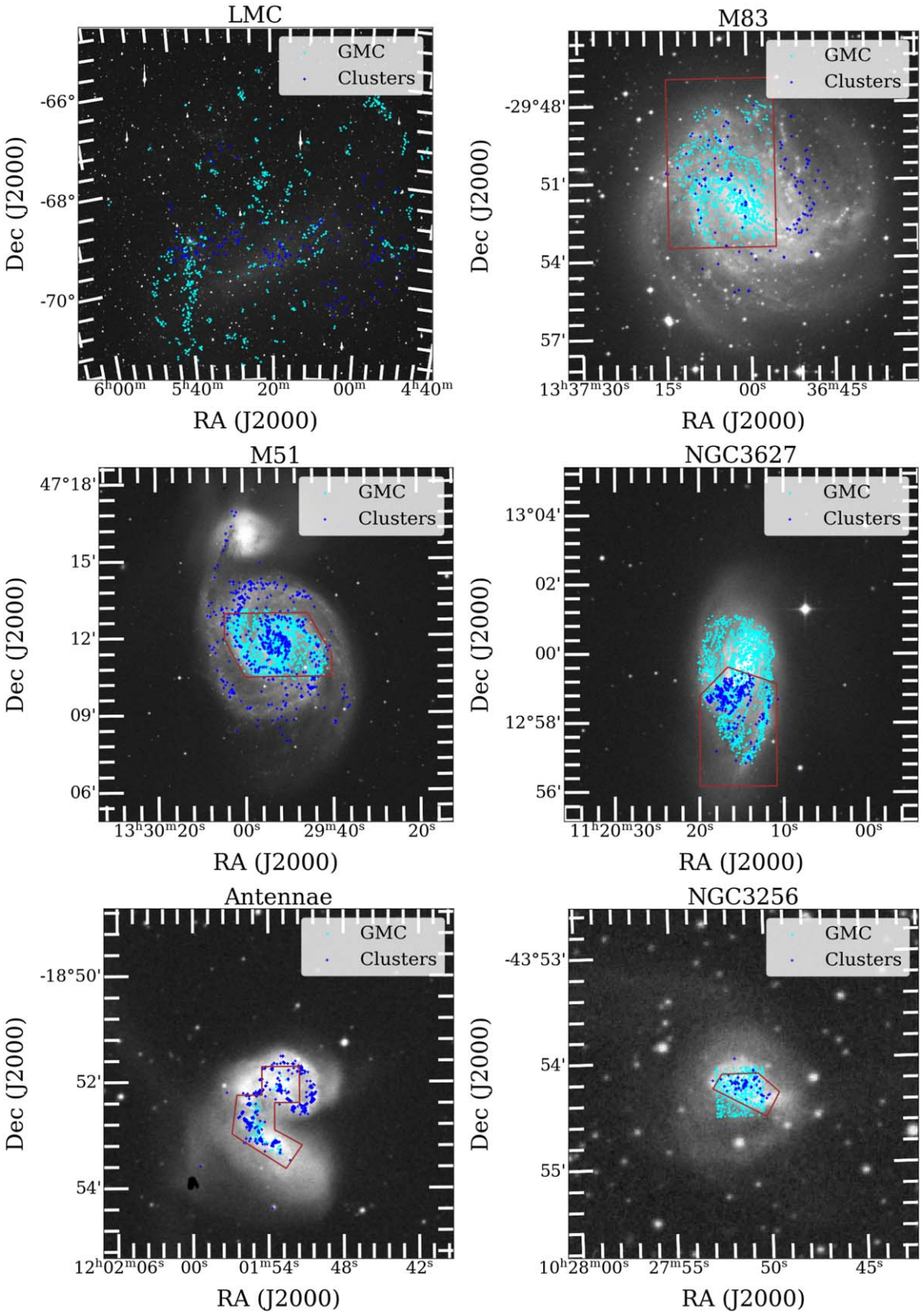

Figure 1. Ground-based images of our galaxy sample, LMC, M83, M51, NGC 3627, the Antennae, and NGC 3256, showing the locations of young star clusters (blue) and GMCs (green). The brown outline shows the area in common between the cluster and GMC catalogs. The images for five galaxies are from the Digital Sky Survey, while the LMC image is retrieved from Karl D. Gordon's website: http://dirty.as.arizona.edu/~kgordon/research/mc/lmc_optical.html.

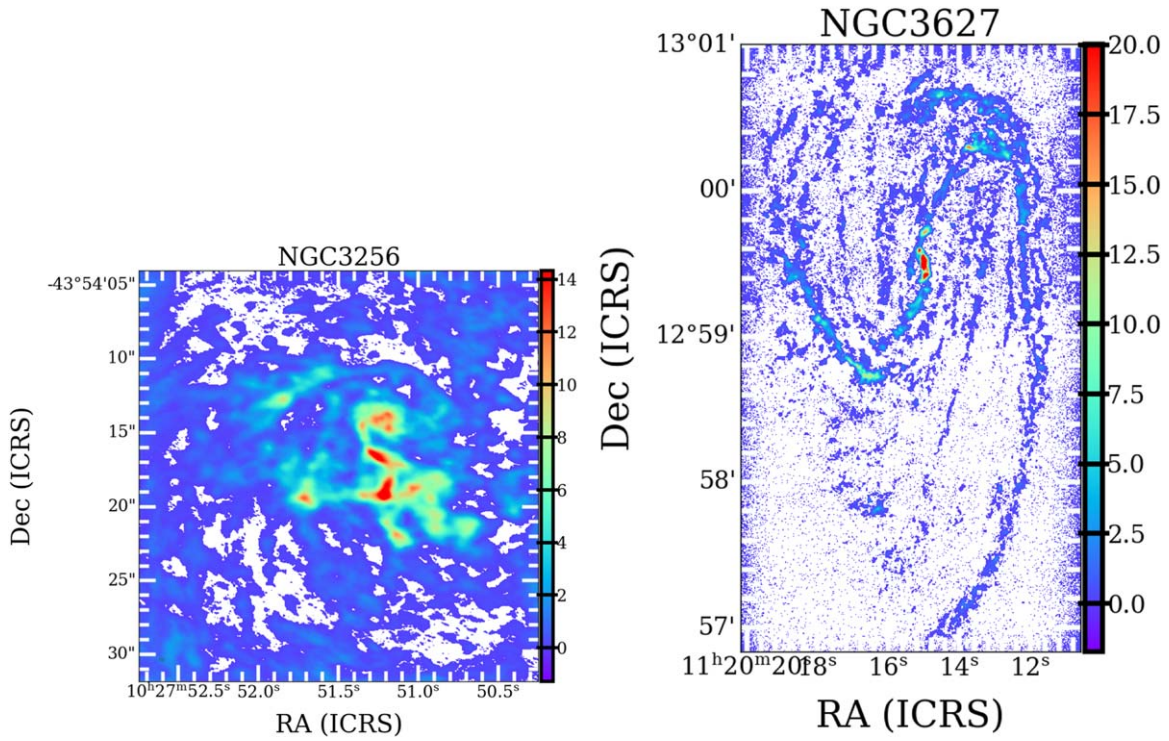

Figure 2. Integrated intensity (moment-zero) maps for the ALMA data sets used for NGC 3256 (left) and NGC 3627 (right). The plots show the integrated CO(2–1) line intensity in units of Jy km s^{-1} bm^{-1}.

Table 1
Summary of the Basic Properties of our Galaxy Sample

Galaxy	Distance (Mpc)	SFR ($M_\odot$ yr^{-1})	$N_{Clusters}$
⋯	⋯	⋯	⋯
LMC	0.050	0.25	931
M83	4.5	2.65	3177
M51	7.6	3.20	3812
NGC 3627	10.1	4.89	742
Antennae	22	20	>10,000
NGC 3256	36	50	505

of twice the measured rms noise. To obtain the final images for NGC 3627, we also run the feathering routine from CASA to incorporate the zero-spacing information from the available single-dish total power observations. The resulting moment-zero (total intensity) maps are presented in Figure 2.

We use the publicly available CPROPSTOO code[3] to detect GMCs (Rosolowsky & Leroy 2006). The routine selects objects that are detected at the $\geqslant 5\sigma$ level in two adjacent channels, where σ is determined from signal-free regions. These regions are then grown to include all pixels with greater than 2σ emission. Our criteria are more strict than the corresponding 2.5σ and 1σ thresholds, respectively, used by Freeman et al. (2017), which leads to fewer detections at the faint end. The difference in methodology has little impact on the resulting mass functions, since those low mass GMCs found in the Freeman et al. (2017) catalog are not used in the fitting process (discussed further in Section 2.3). We also adopt standard values for other CPROPSTOO parameters, such as $\Delta = 2$ in SNR units (which sets the required contrast) and a minimum cloud size of 25 pixels. Tests show that varying the adopted value of Δ (between 1.0 and 3.0) has only a small effect on our conclusions.

For each object, we convert the resulting CO luminosity to H_2 mass by assuming a standard CO-to-H_2 conversion factor of 4.35 $M_\odot$ (K km s^{-1} $pc^2)^{-1}$ and a line ratio between CO(2–1) and CO(1–0) of 0.8 (e.g., Leroy et al. 2009). We also scale the other catalogs to this CO-to-H_2 conversion factor. While this value is appropriate for normal, star-forming galaxies, significantly lower values (such as 0.8 $M_\odot$ (K km s^{-1} $pc^2)^{-1}$) have been suggested for starbursts and Ultra-Luminous Infra-Red Galaxies (ULIRGs); (Bolatto et al. 2013). The two interacting galaxies in our sample, the Antennae and NGC 3256, are both LIRGs and have high rates of star formation. There are also uncertainties in the assumed value of the line ratio used to convert from CO(2–1) to CO(1–0). Previous works have found a range from 0.6 to 1.0 in nearby galaxies (e.g., Leroy et al. 2009). For the Antennae observations, Zaragoza-Cardiel et al. (2014) assume a value of 0.8 to convert from CO(3–2) to CO(1–0), motivated by previous observations (Ueda et al. 2012), and thus we continue to use this value here. The uncertainties associated with the assumed CO-to-H_2 conversion factor, line ratio, and distance to the galaxy do not affect the *shape* of the mass function or the main conclusions of this paper, but will affect the value of M_*.

2.3. Mass Functions

We present binned versions of the GMC mass functions in Figure 3 (red squares). Each distribution appears to follow a power law reasonably well when plotted using equal logarithmic bins, although this binning method can hide weak

[3] http://github.com/akleroy/cpropstoo

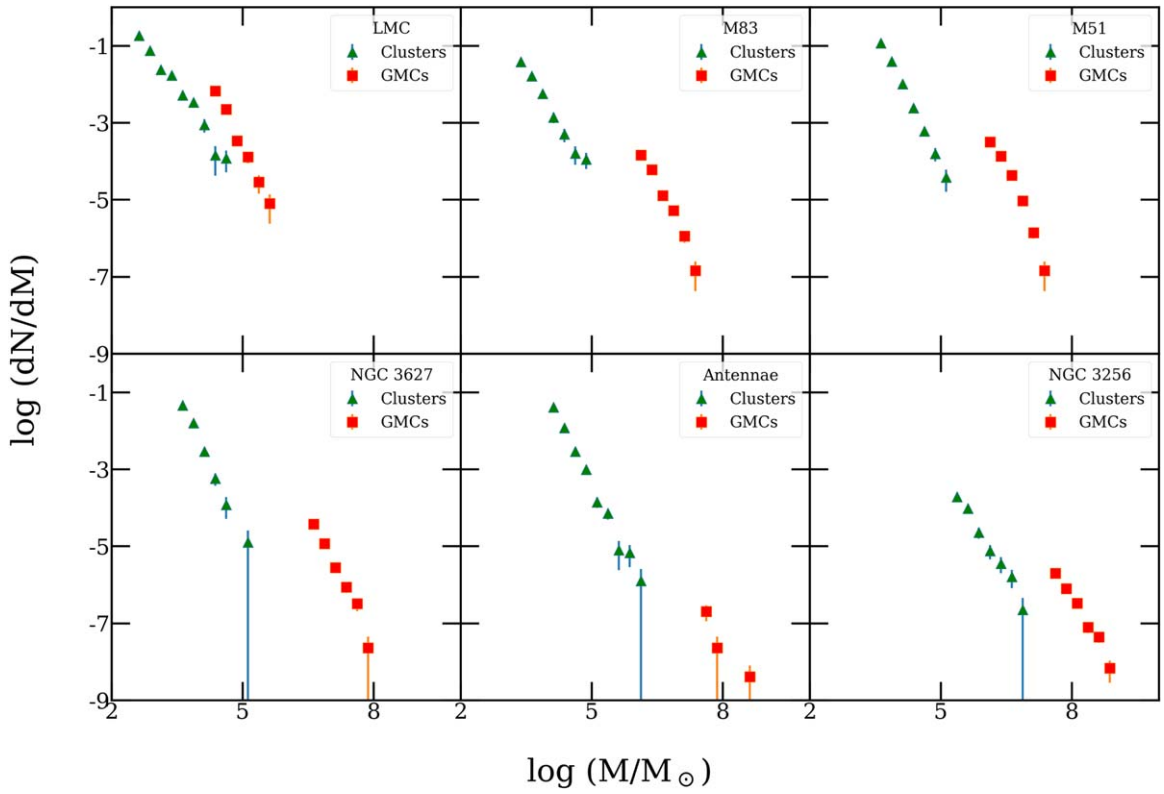

Figure 3. Mass functions of GMCs (red squares) and young (<10 Myr) clusters (blue triangles) plotted using equal logarithmic bins. We only show data above the completeness limit. Note that the binned mass functions shown here are only for visual purposes and are not used in the maximum-likelihood fitting.

Table 2
Summary of the Molecular Gas Observations and GMC Catalogs

Galaxy	Line	α_{CO} ($M_\odot$ (K km s^{-1} pc^2)$^{-1}$)	Line Ratio	Beam (angular) (arcsec)	Beam (physical) (pc)
…	…				
		Previous Work			
LMC (1)	CO(1–0)	4.35	…	45	11
M51 (2)	CO(1–0)	4.35	…	1.16 × 0.97	53 × 36
M83 (3)	CO(1–0)	4.35	…	1.43 × 0.83	29 × 18
Antennae (4)	CO(3–2)	4.35	1.8	0.6 × 1.1	64 × 117
				0.4 × 0.7 (C0)	41 × 62 (C0)
		This Work			
NGC 3627 (5)	CO(2–1)	4.35	0.8	0.95 × 0.88	46 × 43
NGC 3256 (6)	CO(2–1)	4.35	0.8	0.45 × 0.28	78 × 49

Note. C0 indicate properties from the Cycle-0 observations for the Antennae.
References. (1) Wong et al. (2011), (2) Colombo et al. (2014), (3) Freeman et al. (2017), (4) Zaragoza-Cardiel et al. (2014), (5) 2015.1.00956.S (PI: A. Leroy), and (6) 2015.1.00714.S (PI: K. Silwa).

features at the ends of the distribution. We also find that, just as for clusters, the maximum GMC masses approximately scale with their total numbers, as expected from the size-of-sample effect. In Section 4, we will use our maximum-likelihood method to fit a Schechter function to the GMC masses.

It is important to establish a lower mass limit above which each catalog is complete. The fitting procedure can erroneously find a cutoff at higher masses even when there is not one, if sources below the completeness limit (where the distribution flattens) are included. Differences in physical resolution can also potentially affect mass estimates at the lower end of each survey. To minimize the impact of incompleteness and differences in resolution, we apply a uniform procedure (demonstrated in Figure 4) to each GMC and cluster catalog to establish a lower mass limit. This figure shows that the cumulative mass distribution for each GMC catalog follows a power law at the upper end, but eventually flattens toward lower masses. We assume that this flattening is due to incompleteness, rather than to a physical effect, just as we have done previously for cluster catalogs (e.g., Chandar et al. 2017; Mok et al. 2019). We set the completeness limit $M_{\rm lim}$ for each catalog at the mass where the distribution begins to flatten noticeably, represented by the dotted lines in Figure 4, and listed in the second column of Table 3. We show the published

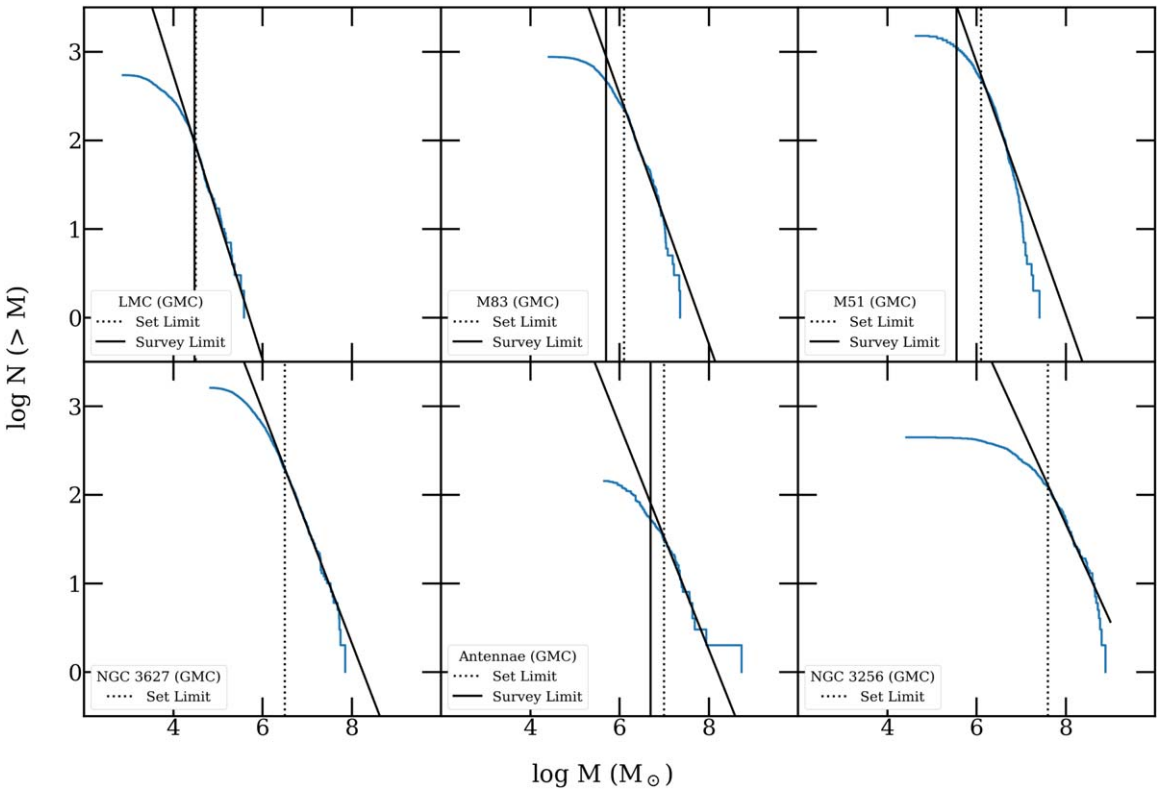

Figure 4. Cumulative distributions of the GMC masses are plotted as the solid blue lines. A power-law fit (black solid line) is added to help guide the eye. The completeness limits determined as described in Section 2.3 are indicated by the dotted vertical lines, and the published completeness limits as solid lines, when available.

completeness limits for comparison, when available, as a solid vertical line. Our method provides stricter lower mass limits than those published for M83, M51, and the Antennae catalogs.

While the galaxies in our sample have a large range of distances, the observations used here (with the exception of the LMC data) all have a physical resolution that is within ∼50% of 50 pc. We tested the potential impact that this range of resolution might have on our results by convolving the NGC 3627 data to match the physical scale of the NGC 3256 catalog, then rerunning it through our detection and fitting software, and found only a small effect on the maximum-likelihood results (described in Section 4). Finally, we note that the GMC data set for the LMC is quite different from the others, since it has significantly higher physical resolution and piecemeal coverage over the galaxy. We present results in this paper for the LMC, but we note that they may not be directly comparable to those from the other five galaxies in the sample.

3. Star Clusters

3.1. Previous Catalogs and Mass Functions

All of the cluster catalogs used in this work, with the exception of that for NGC 3627, have been collected from the literature, and the resulting mass functions published in Chandar et al. (2015, 2017). Here we summarize basic information on each catalog, including where the observations were taken, the cluster selection criteria, and the method for estimating ages and masses.

The LMC cluster catalog is presented by Hunter et al. (2003), and is based on ground-based *UBVR* images taken at the Cerro Tololo Inter-American Observatory. The M51 catalog is presented by Chandar et al. (2016) based on *Hubble Space Telescope* (*HST*) *UBVI*Hα observations. The M83 catalog comes from new *HST UBVI*Hα observations (Whitmore et al. 2020). The Antennae catalog is presented by Whitmore et al. (2010), and is based on *HST UBVI*Hα observations. The cluster catalog for NGC 3256 comes from Mulia et al. (2016), based on *UBVI*Hα *HST* observations. Note that we correct the Antennae and M51 masses by a factor of 0.6 from the original adopted Salpeter (1955) initial mass function (IMF) to a Chabrier (2003) IMF here, which is assumed for the other catalogs.

The clusters in the catalogs used here are all selected to have a higher stellar density than the local background, with no attempt made to assess whether or not they are gravitationally bound based on their morphology, as has been advocated in some works (e.g., Adamo et al. 2017). We believe that this is the best practice when comparing samples of clusters in galaxies with a large range of distances, since morphology cannot be evaluated in a uniform way between the closest and most distant galaxies, which could potentially lead to a distance-related bias. Furthermore, simulations have shown that it is not possible to discern if a cluster is gravitationally bound (has negative or positive energy) based solely on its morphology (e.g., Baumgardt & Kroupa 2007). In Mok et al. (2019), we found that cluster catalogs in M83 and M51 created by different groups, despite having somewhat different methods and criteria, gave similar results for the shape of the mass function.

The age and mass of each cluster is estimated by comparing its integrated multiband photometry with predictions from the Bruzual & Charlot (2003) stellar population models. All galaxies studied here, except the LMC, have narrowband measurements (Hα), which include both stellar continuum and nebular line emission, in their fits. We found that Hα is important in disentangling the effects of age and reddening in the broadband measurements of clusters (e.g., Fall et al. 2005; Whitmore et al. 2020), but also verified that the LMC cluster age estimates are robust (Chandar et al. 2010). To estimate the mass of each cluster, we use the age-dependent mass-to-light ratio and the extinction-corrected V-band magnitude, and we assume an underlying Chabrier (2003) IMF and the distance to each galaxy listed in Table 1. The fitting method typically introduces an uncertainty of 0.3 in log M (≈factor of 2) in the masses (e.g., Elson & Fall 1988; deGrijs & Anders 2006; Chandar et al. 2010).

We compare the mass functions of clusters younger than 10 Myr (blue triangles) in Figure 3 with those of the GMCs in the same galaxies. While it is possible that the cluster mass functions for the most distant galaxies in our sample may suffer from biases related to crowding, previous works have found the shapes of these distributions to be fairly stable out to the distances of ≈40 Mpc. Randriamanakoto et al. (2013) and Mulia et al. (2016) tested the impact of "distance bias" by degrading images of galaxies to simulate distances similar to the two most distant galaxies used here, and found the resulting power-law index of the mass function does not differ by more than ≈0.2.

3.2. New Catalog and Mass Function for NGC 3627

Here, we present a new cluster catalog for NGC 3627 based on broadband images taken in five filters as part of the LEGUS project (UV, UBVI; Calzetti et al. 2015), plus narrowband Hα photometry taken as part of Hα-LEGUS. Nearly 1600 candidate compact clusters were selected following the procedure described in Adamo et al. (2017).

Photometry is performed in a 4 pixel aperture radius for all filters. No continuum subtraction is performed on the narrowband Hα image, so the measurements contain a combination of nebular line and stellar continuum emission. We use two different methods to determine the aperture correction. First, we determine an average aperture correction of 0.834 mag from a number of relatively isolated clusters. Second, we fitted a function to the measured aperture correction and concentration index (C, the difference between aperture magnitudes in 0.5 and 3 pixels; see, for example, Cook et al. 2019) for synthetic clusters. We find that the mass functions are quite similar for both methods of determining aperture corrections. The instrumental magnitudes are converted to the VEGAMAG photometric system by applying zero-points available from the instrument page on the STScI website. We use a similar method to the one described in Section 3.1 to estimate the masses and ages of the clusters.

In Figure 5, we plot the binned mass functions of clusters in NGC 3627 in three different intervals of age: $\tau < 10$ Myr, $\tau = 10$–100 Myr, and $\tau = 100$–400 Myr. The corresponding completeness limits in these age bins are $10^{3.5}\,M_\odot$, $10^{4.2}\,M_\odot$, and $10^{4.5}\,M_\odot$, while the number of clusters above the limits are 289, 44, and 118 respectively. We fitted power laws to the binned distributions, with best-fit indices of -2.49 ± 0.11 ($\tau < 10$ Myr), -1.86 ± 0.20 ($\tau = 10$–100 Myr), and -2.19 ± 0.23 ($\tau = 100$–400 Myr). Note that in the rest of this paper, we only consider clusters with ages younger than 10 Myr.

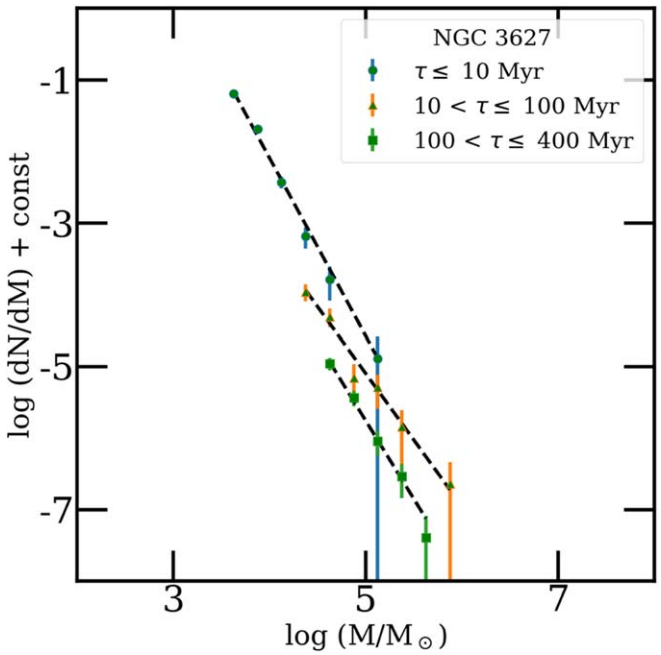

Figure 5. Mass functions of star clusters in NGC 3627 using equal logarithmic bins are plotted in three intervals of age: $\tau < 10$ Myr (circles), $\tau = 10$–100 Myr (triangles), and $\tau = 100$–400 Myr (squares). The dashed lines show the best-fit power law to each distribution, where $dN/dM \propto M^{-\beta_{\rm PL}}$. The best-fit values of $\beta_{\rm PL}$ to the binned points are -2.49 ± 0.11 for $\tau < 10$ Myr, -1.86 ± 0.20 for $\tau = 10$–100 Myr, and -2.19 ± 0.23 for $\tau = 100$–400 Myr.

4. Maximum-likelihood Fits

In this Section, we use the maximum-likelihood method described in Mok et al. (2019) to determine the best-fit values and confidence intervals for the parameters β and M_* when fitting a Schechter function to the cluster and GMC masses above the completeness limit of each catalog. This method has the advantage of not using binned data (which can hide weak features at the ends of the distribution) or cumulative distributions (where the data points are not independent of one another). We compute the likelihood $L(\beta, M_*) = \Pi_i\, P_i$ as a function of β and M_*, where the probability P_i for each cluster is given by

$$P_i = \frac{\psi(M_i)}{\int_{M_{\rm min}}^{\infty} \psi(M) dM}, \tag{1}$$

and the product is over all GMCs or clusters above $M_{\rm min}$ (see, e.g., Chapter 15.2 of Mo et al. 2010). For each catalog, we set the upper integration limit in Equation (1) to be 100 times the mass of the most massive cluster in that sample; our tests showed that this was sufficient for convergence in all cases. Next, we find the maximum-likelihood $L_{\rm max}$ using the Nelder & Mead (1965) method, and use the standard formula

$$\ln L(\beta, M_*) = \ln L_{\rm max} - \frac{1}{2}\chi_p^2(k), \tag{2}$$

Table 3
GMC Mass Function Parameters, with $\sigma(\log M) = 0.0$

Galaxy	$\log M_{\rm lim}$	$\log M_{\rm max}$	Num	$-\beta$	$\log M_*$	$-\beta_{\rm PL}$
LMC	4.5	5.59	86	2.47 [1.85, 2.95]	5.78 [5.15, 9.00]	2.68 [2.50, 2.85]
M83	6.1	7.36	223	1.83 [1.45, 2.15]	7.05 [6.80, 7.50]	2.35 [2.25, 2.45]
M51	6.1	7.41	490	1.22 [0.90, 1.50]	6.66 [6.55, 6.80]	2.33 [2.25, 2.40]
NGC 3627	6.5	7.85	189	1.98 [1.65, 2.25]	7.72 [7.40, 8.45]	2.30 [2.20, 2.40]
Antennae[a]	7.0	8.74	30	2.20 [1.70, 2.55]	9.00 [8.25, 9.00]	2.23 [2.00, 2.45]
NGC 3256	7.6	8.89	123	1.61 [1.25, 1.95]	8.71 [8.40, 9.00]	2.10 [2.00, 2.20]

Notes. Square brackets indicate 1σ confidence intervals.
[a] Indicates that the Nelder–Mead routine converged to a value beyond the adopted grid. The maximum-likelihood value found in the grid is adopted instead.

where $\chi^2_p(k)$ is the chi-squared distribution with k degrees of freedom at p confidence level, to determine the 1, 2, and 3σ confidence contours. We present our results for the zero-error case in Section 4.1 and for the case including a typical uncertainty of $\sigma(\log M) = 0.3$ in Section 4.2.

4.1. Results without Measurement Uncertainties

Figure 6 shows the best-fit values of β and M_* (dashed lines) for the GMCs (top panels) and clusters (bottom panels), when no uncertainties in the measurements are included. The shaded regions show the 1, 2, and 3σ contours resulting from our maximum-likelihood fit. The best-fit values of β and M_* and their 1σ uncertainties are also listed in Table 3 for GMCs and in Table 4 for clusters. Most of the contours have a diagonal portion, which indicates the trade-off between a steeper value of β and a higher cutoff mass M_* and vice versa. There is also a relatively flat portion for some galaxies at higher values of M_*, i.e., as the mass function approaches a pure power law.

Our results for the GMCs (shown in the top set of panels in Figure 6) can be broadly classified into three groups. For the LMC, the Antennae, and NGC 3256, the 1σ contours (darkest region) remain open up to the right edge of the diagram, i.e., up to the maximum tested value of M_*. This means that the value of M_* is indeterminant and the upper portion of the mass function is consistent with a pure power law. We note that the large allowable range in M_*, particularly for the LMC and the Antennae, is at least partly driven by the relatively small number of GMCs in those catalogs. For M83 and NGC 3627, the 3σ and 2σ contours, respectively, remain open up to the maximum tested value for M_*. In these cases, the GMC masses are also consistent with being drawn from a pure power law (not excluded at $> 3\sigma$ significance), but with some weak evidence for a physical cutoff. M51 is the only galaxy in our sample that shows evidence for an upper cutoff in the mass function of its GMCs at greater than 3σ significance.

We present the results for clusters younger than 10 Myr in the bottom set of six panels in Figure 6. We previously presented results from our maximum-likelihood fitting for the cluster populations in all galaxies (except for NGC 3627) in three intervals of age: <10, 10–100, and 100–400 Myr (Mok et al. 2019). As discussed in that work, ideally we should find consistent results for the Schechter parameters β and M_* between all three age intervals, because we do not expect the physics of cluster formation to change significantly over such a short time period (only ~3% of the Hubble age). However, systematic errors can affect the mass estimates differently in the different age intervals.

For M83, the Antennae, and NGC 3256, the 1σ contours remain open up to the right edge of the diagram. M51 and NGC 3627 are consistent with a power law, but also show some weak evidence for a cutoff. The only galaxy with $>3\sigma$ evidence for an exponential cutoff M_* in its young cluster population is the LMC, but no cutoff is found in the older populations (Mok et al. 2019). We conclude that physical cutoffs appear to be the exception rather than the rule in the mass functions of GMCs and young clusters in our sample.

4.2. Results with Measurement Uncertainties

Thus far, we have neglected uncertainties in the mass estimates of clusters and GMCs. We assess the impact that observational uncertainties have on our results for β and M_* by repeating our maximum-likelihood analysis after convolving the Schechter function with a log-normal error distribution of width 0.3 in $\log M$. This is the typical uncertainty found in mass estimates of GMCs in M51 (see Section 2.1), and for stellar clusters (see Section 3.1). We follow the procedure for including measurement uncertainties outlined in Efstathiou et al. (1988) and described in detail in the Appendix. The main effect of including uncertainties using this method is to modify the shape of the Schechter function such that it more closely resembles a power law, with the exponential cutoff shifting to a higher mass (see Figure 9). This procedure, however, leaves a power-law mass function invariant, including the index $\beta_{\rm PL}$.

In Figure 7, we show the results of our maximum-likelihood fits when uncertainties of 0.3 in $\log M$ are included. The corresponding best-fit values of M_* and $\beta_{\rm PL}$ are listed in Table 5 for GMCs and in Table 6 for clusters. Compared with the zero-error case, the confidence contours increase in size, allowing for a larger range and hence correspondingly weaker constraints on the power-law index β and cutoff mass M_*. The GMC mass functions in our sample do not show evidence for M_*, with the exception of M51. In this case, including uncertainties in the fit still results in a detection of M_* at the $>3\sigma$ level, but with a lower best-fit value for M_*.

For the cluster populations, a similar behavior occurs, where including uncertainties lowers the best-fit values of M_* in M51 and NGC 3627. This happens because a Schechter function convolved with the error distribution has a shape closer to that of a power law, which shifts the best-fit M_* to a lower value in order to compensate for this behavior. While accounting for observational uncertainties using our simple prescription results in a detection of M_* in the *cluster* population of NGC 3627, no corresponding detection is made for GMCs in this galaxy. M51 remains the only galaxy in our sample with evidence for a high-mass cutoff in both the GMC and young cluster populations.

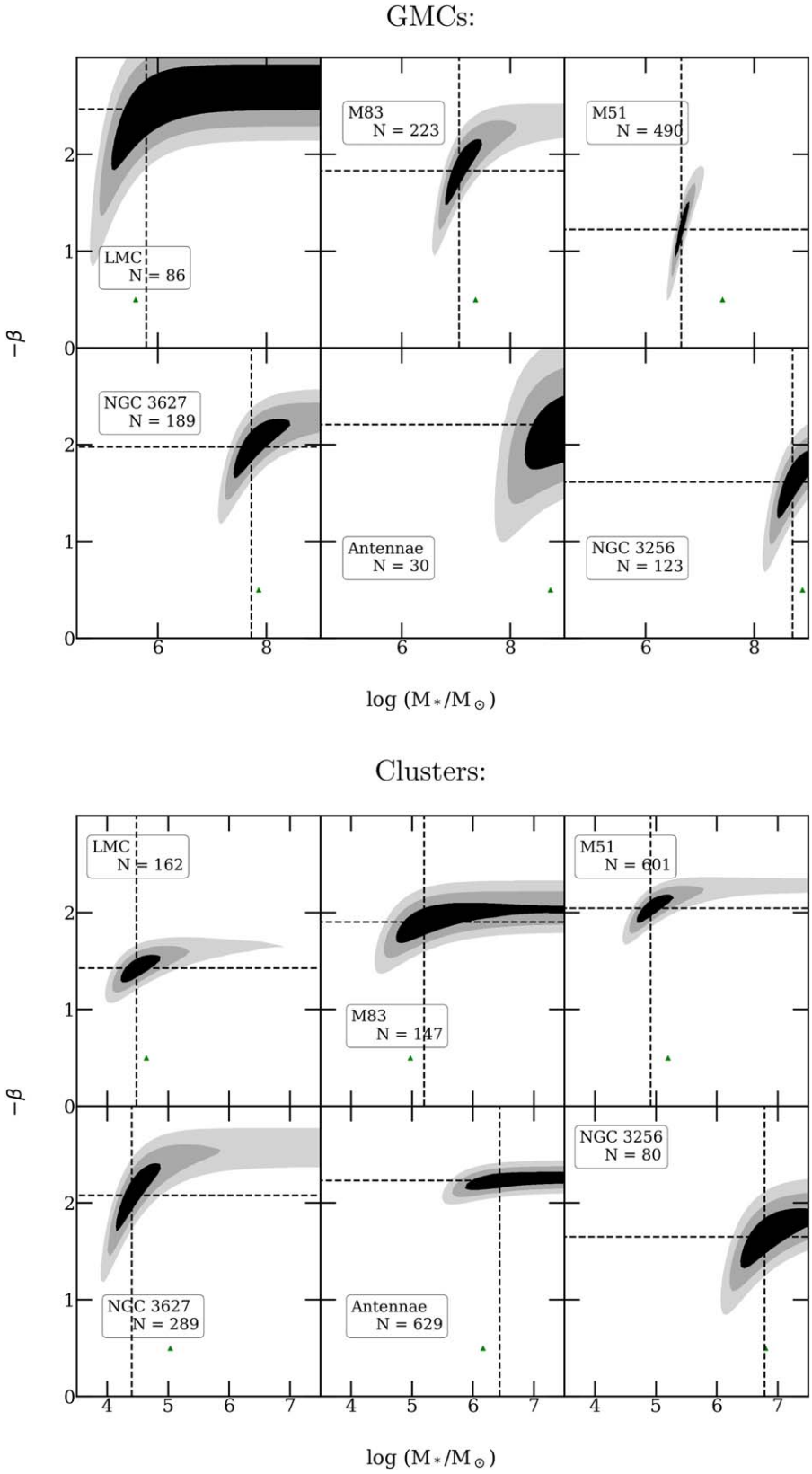

Figure 6. The top panels show the results of our maximum-likelihood fits for the Schechter parameters β and M_* to the GMC populations of our sample galaxies, and the bottom panels show the results for the young ($\tau < 10$ Myr) cluster populations. No measurement uncertainties are included in the fitting. The dashed lines show the best-fit values of β and M_*, while the boundaries of the shaded regions show the 1, 2, and 3σ confidence contours. The small triangles indicate the most massive GMC or cluster in each catalog.

Table 4
Cluster Mass Function Parameters, with $\sigma(\log M) = 0.0$

Galaxy	$\log M_{\rm lim}$	$\log M_{\rm max}$	Num	$-\beta$	$\log M_*$	$-\beta_{\rm PL}$
LMC	2.5	4.64	162	1.42 [1.25, 1.55]	4.48 [4.20, 4.90]	1.67 [1.60, 1.70]
M83	3.3	4.97	147	1.90 [1.70, 2.10]	5.20 [4.75, 7.50]	2.04 [1.95, 2.10]
M51	3.5	5.20	601	2.04 [1.90, 2.20]	4.92 [4.70, 5.30]	2.28 [2.25, 2.35]
NGC 3627	3.5	5.04	289	2.08 [1.70, 2.40]	4.41 [4.15, 4.90]	2.56 [2.50, 2.65]
Antennae	4.0	6.17	629	2.23 [2.15, 2.30]	6.44 [5.85, 7.50]	2.26 [2.20, 2.30]
NGC 3256	5.2	6.80	80	1.65 [1.30, 1.95]	6.78 [6.40, 7.50]	1.93 [1.85, 2.05]

Note. Square brackets indicate 1σ confidence intervals.

Table 5
GMC Mass Function Parameters, with $\sigma(\log M) = 0.3$

Galaxy	$\log M_{\rm lim}$	$\log M_{\rm max}$	Num	$-\beta$	$\log M_*$
LMC	4.5	5.59	86	2.41 [1.20, 2.90]	5.44 [4.50, 9.00]
M83	6.1	7.36	223	1.55 [0.60, 2.10]	6.61 [6.20, 7.15]
M51[a]	6.1	7.42	490	0.00 [0.00, 0.75]	5.95 [6.00, 6.25]
NGC 3627	6.5	7.85	189	1.84 [1.20, 2.25]	7.34 [6.85, 8.15]
Antennae[a]	7.0	8.74	30	2.20 [1.35, 2.55]	9.00 [7.55, 9.00]
NGC 3256	7.6	8.89	123	1.50 [0.75, 1.95]	8.43 [8.00, 9.00]

Notes. Square brackets indicate 1σ confidence intervals.
[a] Indicates that the Nelder–Mead routine converged to a value beyond the adopted grid. The maximum-likelihood value found in the grid is adopted instead.

Table 6
Cluster Mass Function Parameters, with $\sigma(\log M) = 0.3$

Galaxy	$\log M_{\rm lim}$	$\log M_{\rm max}$	Num	$-\beta$	$\log M_*$
LMC	2.5	4.64	162	1.39 [1.20, 1.55]	4.30 [3.95, 4.75]
M83	3.3	4.97	147	1.88 [1.60, 2.10]	4.99 [4.40, 7.50]
M51	3.5	5.20	601	1.87 [1.55, 2.10]	4.43 [4.10, 4.85]
NGC 3627[a]	3.5	5.04	289	0.00 [0.00, 1.50]	3.50 [3.50, 3.80]
Antennae	4.0	6.17	629	2.19 [2.05, 2.30]	6.04 [5.40, 7.50]
NGC 3256	5.2	6.80	80	1.60 [1.10, 1.95]	6.56 [6.00, 7.50]

Notes. Square brackets indicate 1σ confidence intervals.
[a] Indicates that the Nelder–Mead routine converged to a value beyond the adopted grid. The maximum-likelihood value found in the grid is adopted instead.

4.3. Schechter Function versus Power-law Fits

Since we do not find a physical cutoff for most of the galaxies in our sample, we also apply our maximum-likelihood fitting routine for the case where $M_* \rightarrow \infty$, i.e., fitting a pure power law to the data. We list the best-fit power-law index $\beta_{\rm PL}$ in the last column of Tables 3 and 4. In every case, the fitting returns a steeper value for $\beta_{\rm PL}$ compared with the best-fit index β for the Schechter case. This is due to the correlation between β and M_*, which leads to flatter values of β when an underlying Schechter function is assumed. Therefore, caution should be used when comparing results from different works, since adopting different underlying functions (pure power law versus Schechter versus truncated power law) can lead to different values of the power-law index.

We perform statistical tests to assess if one of the underlying distributions (power law or Schechter) gives a better description of the data. We calculate the Akaike Information Criterion (AIC; Akaike 1974), given by $\mathrm{AIC} = 2k - 2\ln L_{\rm max}$, where k is the number of parameters and $L_{\rm max}$ is the maximum value of the likelihood function. A lower AIC value indicates a better description of the data. The results for young ($\tau < 10$ Myr) clusters and GMCs are compiled in Table 7 for the case without measurement uncertainties. We also compile results from the relative likelihood test (Burham & Anderson 2002), given by $\exp((\mathrm{AIC}_1 - \mathrm{AIC}_2)/2)$, which is the probability that the less likely model *also* minimizes the information and provides a good description of the data. Lower values from the relative likelihood test indicate a stronger preference for the model with a lower AIC value. We adopt a likelihood value of 0.05 or less (corresponding to $\approx 2\sigma$) as suggesting a preference for one model over the other. For clusters, the results indicate a weak preference for a Schechter function in the LMC and M51. For GMCs, the results suggest a strong preference for an underlying Schechter function in M51 and a weak preference in M83. These results largely agree with our qualitative discussion above of the maximum-likelihood fits.

For GMCs, when a Schechter function is assumed to describe the mass function, the best-fit β values in our galaxy sample range from -1.22 to -2.47 with a median $\beta \approx -2.2$. When we use a power law instead, the best-fit $\beta_{\rm PL}$ values range

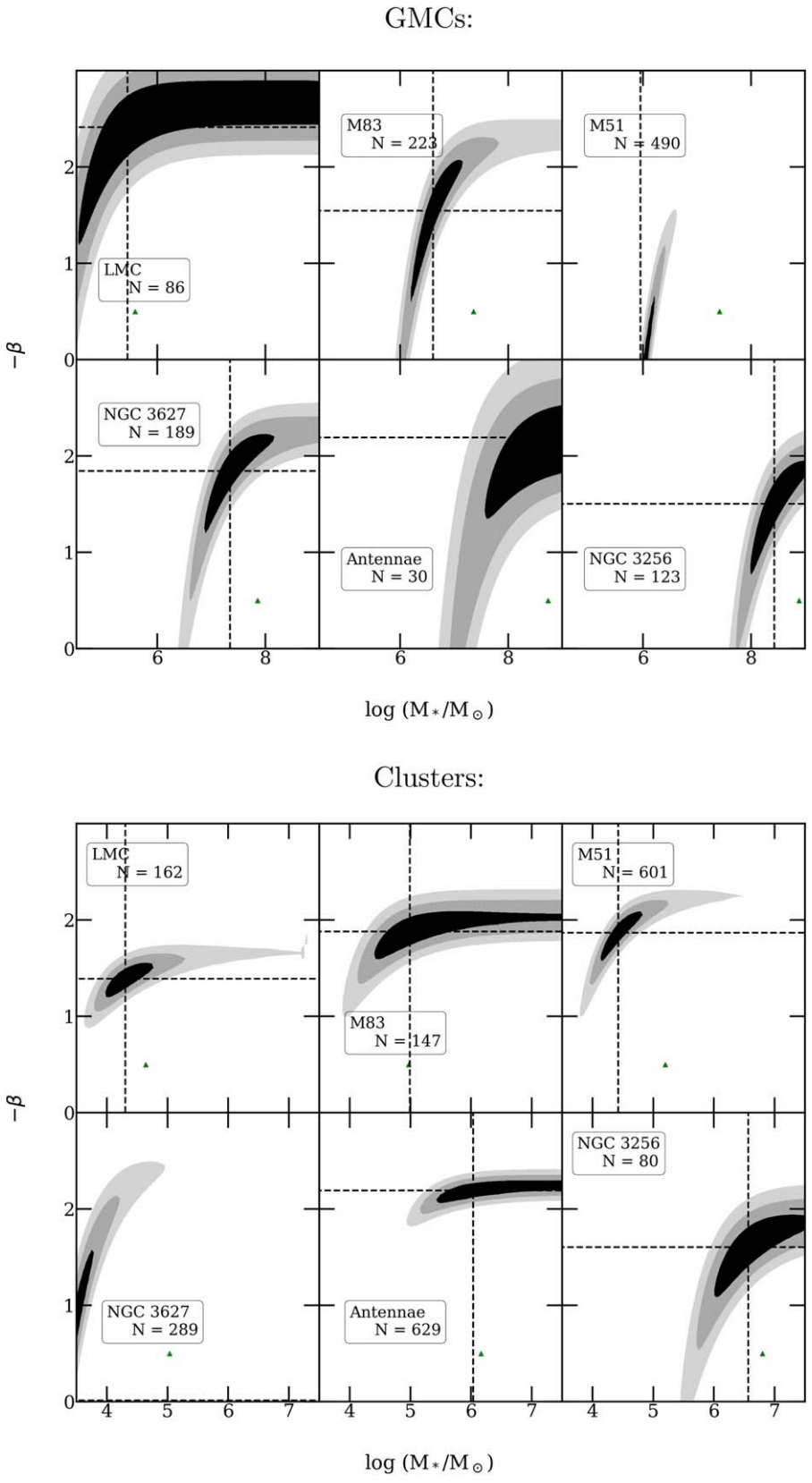

Figure 7. Same as Figure 6, but we fit with a Schechter function convolved with a log-normal error distribution with dispersion $\sigma(\log M) = 0.3$.

from -1.93 to -2.68 with a median $\beta_{\rm PL} \approx -2.3$ and a standard deviation of $\approx$0.3. Thus for our galaxy sample, we find $\beta_{\rm PL} = -2.3 \pm 0.3$ for GMC mass functions.

For young clusters, we find best-fit β values (with an underlying Schechter function) that range from -1.42 to -2.23 with a median $\beta \approx -1.9$, and $\beta_{\rm PL}$ values (power law) from

Table 7
AIC and Relative Likelihood Values

Clusters	AIC_{PL}	AIC_{Sch}	Rel.
LMC	2801	**2791**	6×10^{-3}
M83	2806	**2805**	9×10^{-1}
M51	11540	**11,532**	2×10^{-2}
NGC 3627	5353	**5348**	8×10^{-2}
Antennae	**13,549**	13,550	6×10^{-1}
NGC 3256	**2272**	2270	5×10^{-1}
GMCs	AIC_{PL}	AIC_{Sch}	Rel.
LMC	**1973**	1975	5×10^{-1}
M83	6913	**6906**	4×10^{-2}
M51	15211	**15,165**	1×10^{-10}
NGC 3627	6230	**6227**	3×10^{-1}
Antennae	**1069**	1071	3×10^{-1}
NGC 3256	4754	**4749**	8×10^{-2}

Note. Bolded values indicate the lower value of the AIC. The relative likelihood test shows the probability that the less likely model also minimizes information loss.

-1.67 to -2.56 with a median $\beta_{PL} \approx -2.0$ and standard deviation ≈ 0.3. Therefore, we find $\beta_{PL} = -2.0 \pm 0.3$ for the cluster mass functions.[4]

5. Discussion

5.1. The Shape of the GMC Mass Functions

Earlier studies have found a large range for the power-law index of GMC mass functions in nearby galaxies, from $\beta_{PL} = -1.5$ in the inner disk of the Milky Way (Rice et al. 2016) to $\beta_{PL} = -2.6$ in the LMC (Wong et al. 2011) and $\beta_{PL} = -2.9$ in M33 (Rosolowsky 2005). There are also some discrepancies among the published indices, such as $\beta_{PL} = -1.7$ for the LMC (Blitz et al. 2007) and $\beta_{PL} = -2.3$ for M33 (Gratier et al. 2012). Some of these discrepancies may be caused by different underlying assumptions, observational techniques, and fitting methods. Thus, from earlier work it is unclear if the mass functions of GMCs have similar or different shapes from one galaxy to another.

In this work, we have applied a uniform methodology to fit the mass functions of GMCs and young clusters in six star-forming galaxies (LMC, M83, M51, NGC 3627, the Antennae, and NGC 3256), which includes irregulars, spirals, and mergers, and dwarf and massive galaxies. One of our main results is that a pure power law provides a good fit to the mass functions of GMCs for all but one galaxy (M51) in our sample. We also find a relatively small range for the power-law index, $\beta_{PL} = -2.3 \pm 0.3$, indicating that the shapes of GMC mass functions are fairly similar among the galaxies in our sample.

Overall, we find good agreement when we compare our fitting results for GMC catalogs in the LMC, M83, and M51 with previously published ones. For the LMC and M51, previous works have fitted a truncated power law of the form $N(M' > M) = N_o[(M/M_o)^{\beta+1} - 1]$ (Rosolowsky 2005), which returns a truncation mass M_o and the statistic N_o (values of N_o significantly larger than 1 indicate that a cutoff is preferred over a power law). For the LMC, Wong et al. (2013) found $N_o = 0.15 \pm 1.48$ using the same catalog used in this paper, i.e., no cutoff was detected, similar to our result. They also found $\beta = -2.57 \pm 0.20$, similar to our best fits of $\beta = -2.47$ and $\beta_{PL} = -2.68$. For M51, Colombo et al. (2014) found $N_o = 17 \pm 7$ ($\approx 2.5\sigma$ significance), $M_o = (18.5 \pm 3.4) \times 10^6\ M_\odot$, and $\beta = -2.29 \pm 0.09$. The maximum-likelihood method used here also supports a truncation in the GMC mass function in M51, but with a somewhat lower cutoff value ($M_* = 4.6 \times 10^6$ versus $M_o = 1.9 \times 10^7$), possibly due to the different assumed functional form. For M83, Freeman et al. (2017) did not present results for the entire GMC sample, instead focusing on fits in six radial bins, but their results appear to be consistent with our weak indication for a physical cutoff.

5.2. GMCs versus Clusters

A comparison between the shapes of GMCs and clusters in the same galaxies provides important clues to the processes that operate during cluster formation and early evolution. If the shapes of the mass functions of GMCs and clusters are similar, this implies that the SFE has little or no dependence on the mass of the protoclusters. A comparison of the normalizations between the GMC and cluster mass functions (in the same galaxy) would then provide a numerical estimate of the SFE. Unfortunately, the available data sets are too heterogeneous and include molecular gas observations with different CO transitions, different angular and physical resolutions, and different sky coverage of the GMC and cluster maps, which all introduce significant uncertainties in the normalization of the GMC mass function. Thus, we do not attempt to estimate numerical values for the star formation efficiencies in this paper.

As clusters form, the energy and momentum injected by young stars eventually expel the remaining gas and halts further star formation. Several feedback mechanisms (e.g., protostellar jets and outflows, radiation pressure, photoionized gas, and supernovae) likely operate simultaneously during these early phases. Radiative losses inside the young clusters determine how much of the energy from stellar feedback is available to remove the gas. The FKM model describes two extreme regimes that likely encompass most realistic situations: the energy-driven regime, where there are no radiative losses, so all of the feedback energy stays in the region and is available to expel the ISM, and the momentum-driven regime, where there

[4] In our previous papers characterizing cluster systems, we found uncertainties closer to $\sim \pm 0.2$ for β_{PL}. Here, we find a somewhat larger uncertainty because of the smaller number of measurements, i.e., we determine β_{PL} for a single age range ($\tau < 10$ Myr) rather than all three age ranges.

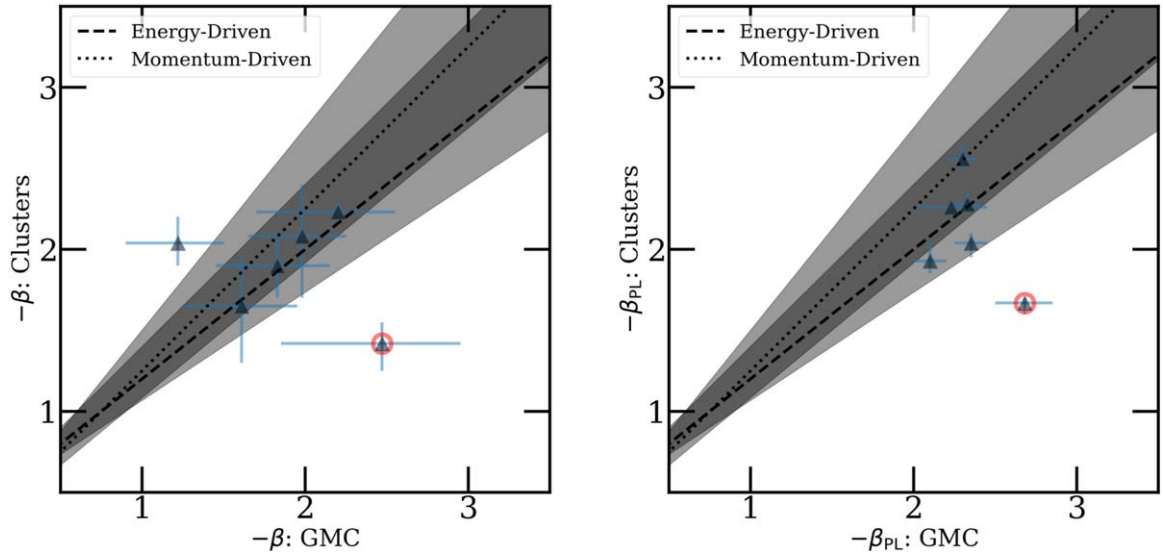

Figure 8. A comparison of the best-fit power-law indices ($-\beta$) in the mass functions of GMCs and young ($\tau < 10$ Myr) clusters. The left panel shows the results when we assume an underlying Schechter function, and the right panel shows the results when an underlying power law is assumed. The results for the LMC are circled in red, since this galaxy has more piecemeal coverage and significantly higher resolution than the others, as described in the text. The dashed and dotted lines show predictions for the relation between β_C and β_{GMC} in the energy-driven and momentum-driven feedback regimes, where the exponent of the index of the mass–radius relation of the protoclusters is assumed to be $\alpha = 0.5$ (see Section 5.2). The shaded regions show the predictions when uncertainties of ± 0.1 are allowed on α.

are maximum radiative losses. In the model, the mass–radius relation of the protoclusters is approximated by a power law, $R_h \propto M^{\alpha}$. Studies in the Milky Way and LMC of star-forming clumps (e.g., FKM; Wu et al. 2010; Wong et al. 2019) and GMCs (Larson 1981; Blitz et al. 2007) indicate $\alpha \approx 0.5$. FKM derived the following relations between the power-law indices of the mass functions of the gas-dominated protoclusters (G) and the resulting stellar clusters (S) for the energy-driven case:

$$\beta_S = \frac{2(\beta_G + \alpha - 1)}{5(1 - \alpha)}, \quad (3)$$

and the following relation for the momentum-driven case:

$$\beta_S = \frac{2\beta_G + \alpha - 1}{4(1 - \alpha)}. \quad (4)$$

Strictly speaking, the gas-dominated protoclusters in the model correspond most directly to dense, star-forming clumps within GMCs rather than to the GMCs themselves. However, the clump mass function can also be fitted by a power-law function with $\beta_{PL} \approx 1.7$ (e.g., Wong et al. 2008). Since GMCs and clumps have similar mass functions and mass–radius relations, it is likely that the scaling relations for the power-law indices of the mass functions in Equations (3) and (4) derived in the simple feedback model apply at least approximately to both types of clouds. Therefore, in Figure 8, we plot the predicted FKM relations on top of the comparison of β_S and β_G in our sample.

We also note that in the FKM model, the SFE (ϵ) in protoclusters depends primary on their mean surface density (Σ). One important consequence of this relation is that if Σ is roughly constant from one protocluster to another, then ϵ will also be roughly constant and the power-law indices of the mass functions of molecular clouds and young star clusters will be similar (the case of $\alpha = 0.5$ discussed above). Recent observations of clouds in nearby galaxies, such as the sample of 15 galaxies compiled in Sun et al. (2018) from the PHANGS survey and archival sources, show large variations in Σ among galaxies, ranging from $\sim 10^1$ to $\sim 10^4\, M_\odot$ pc^{-2}. However, if we restrict attention to the clouds within any single galaxy (excluding clouds near the center), then the distribution of Σ is much narrower, consistent with the FKM model; see Figures 1 and 2 in Sun et al. (2018). Given that we apply the FKM model to each galaxy on an individual basis, this framework is valid for the analysis presented here.

We see that the momentum-driven regime (dotted line) predicts a somewhat steeper relation between the power-law indices of clusters and GMCs (in the sense that the clusters are predicted to have steeper distributions) than the energy-driven regime (dashed line). We also show uncertainties of ± 0.1 on α as the shaded regions. We plot our best-fit results for β (with an underlying Schechter function) on the left and for β_{PL} (with an underlying power law) on the right in Figure 8. The LMC is an outlier in this plot, possibly due to the partial coverage and significantly higher physical resolutions. Our results for the other five galaxies are largely consistent with either set of predictions, but the sample is fairly small. We find tentative signs that the mass functions of GMCs may be slightly steeper than those of clusters in the same galaxies, with $\beta_{PL} = -2.3 \pm 0.3$ for GMCs and $\beta_{PL} = -2.0 \pm 0.3$ for clusters, but overall we find that $\beta_{Clusters} \approx \beta_{GMC} \approx -2$. The similarity in the shapes of the mass functions of GMCs and young clusters suggests that the SFE for the clusters in our sample is largely independent of the cloud or protocluster mass, consistent with the FKM model.

5.3. SFE and M_*

Previous works have estimated the SFE in GMCs from the ratio of the upper cutoffs in cluster and GMC mass functions (e.g., Freeman et al. 2017; Messa et al. 2018a). Note that many of the previous works on this topic have adopted a truncated power law instead of a Schechter function, but the general results are similar (see Section 5.1). We will continue to use the terminology of M_* to denote a steep decline at the high mass end (i.e., a physical cutoff). Messa et al. (2018a) found a ratio

of ∼1%, which they attributed to a combination of a ∼10% SFE plus ∼10% of stars surviving in bound clusters.

Our results suggest, however, that physical upper cutoffs may be the exception rather than the rule. In cases where M_* is indeterminant or only weakly detected, this method for estimating the SFE is unreliable. The method becomes even more problematic when studying parts of galaxies, where smaller samples result in larger uncertainties in the fitted parameters. In the ideal case, where there is strong evidence for physical upper mass cutoffs in both the GMC and cluster mass functions, the ratio would represent a real relation between the two populations. However, the results from our sample indicate that this may not be the case for most galaxies.

6. Conclusions and Summary

In this paper, we measure the shapes of the mass functions of GMCs and young clusters (ages <10 Myr) in six star-forming galaxies: LMC, M83, M51, NGC 3627, the Antennae, and NGC 3256. These galaxies span a large range in distance (from ∼50 kpc to ∼40 Mpc), SFR (∼0.25 to ∼50 $M_\odot$ yr^{-1}), and morphology (irregulars, spirals, and mergers). For NGC 3627, we present a new GMC catalog based on archival ALMA observations and a new cluster catalog from the *HST*-based LEGUS and Hα-LEGUS projects. We also present a new catalog of GMCs in the merging NGC 3256 system based on archival ALMA observations. We perform maximum-likelihood fits of the Schechter function ($dN/dM \propto M^\beta \exp(-M/M_*)$) and a pure power law ($dN/dM \propto M^{\beta_{\rm PL}}$) to the observed GMC and cluster mass functions in a uniform way, using the procedure from Mok et al. (2019). Our main conclusions are as follows:

1. We find that, to first order, the majority of the GMC mass functions studied here are consistent with having a power-law index $\beta_{\rm PL} = -2.3 \pm 0.3$. The uncertainties on each $\beta_{\rm PL}$ are large enough that there may be real variations among galaxies, although the range found here is not as large as the full range of $\beta_{\rm PL}$ values found in the earlier studies. We find that the mass functions of young clusters in our sample can be described by $\beta_{\rm PL} = -2.0 \pm 0.3$.
2. For almost all of our target galaxies (5/6), we find little or no evidence for a physical upper cutoff in the mass function of GMCs. This suggests that such cutoffs may be the exception, rather than the rule, in populations of GMCs in nearby galaxies. Previously, we found a similar result for young cluster populations in a sample of eight galaxies, i.e., that most of their mass functions do not show evidence for a physical cutoff at the high end M_* (Mok et al. 2019). M51 is the only galaxy in our sample that shows evidence for a physical upper mass cutoff in both the GMC and young cluster populations.
3. In general, we find $\beta_{\rm GMC} \approx \beta_{\rm C} \approx -2$. This is consistent with predictions of the analytic FKM model. Since the shapes of the two mass functions are fairly similar, this indicates that the SFE is largely independent of protocluster mass.
4. Given the lack of strong cutoffs in our sample, the method of estimating the SFE in a galaxy from the ratio of the cutoff mass (M_*) in the cluster to that in the GMC populations may not be applicable except in rare cases.

Our results are based on the GMC and cluster populations in a relatively small number of galaxies. We plan to confirm these results in larger samples of galaxies when the data become available. Since it is possible that resolution-dependent and other observational biases may affect the observed shape of the distribution, we believe another important step is to collect higher resolution observations of molecular gas, particularly at the clump scale. Observations of very nearby galaxies or simulated galaxies could also be degraded to simulate a range of different distances, in order to test its impact on the shape of the mass function.

R.C. acknowledges support from NSF grant 1517819. The authors acknowledge the helpful comments provided by the referee, Erik Rosowlowsky.

The Digitized Sky Surveys were produced at the Space Telescope Science Institute under U.S. Government grant NAG W-2166. The images of these surveys are based on photographic data obtained using the Oschin Schmidt Telescope on Palomar Mountain and the UK Schmidt Telescope. The plates were processed into the present compressed digital form with the permission of these institutions.

This paper makes use of the following ALMA data: ADS/JAO.ALMA#2015.1.00956.S and ADS/JAO.ALMA#2015.1.00714.S. ALMA is a partnership of ESO (representing its member states), NSF (USA), and NINS (Japan), together with NRC (Canada), *MOST* and ASIAA (Taiwan), and KASI (Republic of Korea), in cooperation with the Republic of Chile. The Joint ALMA Observatory is operated by ESO, AUI/NRAO, and NAOJ.

Appendix
Maximum-likelihood Method with Errors

To include measurement errors in our maximum-likelihood fits of the Schechter mass function to GMC and cluster catalogs, we follow the treatment in Efstathiou et al. (1988), who fitted Schechter luminosity functions to galaxy catalogs. As in the error-free case, we adopt the Schechter function (ψ_t) as the true underlying mass function of GMCs and clusters:

$$\psi_t(M) = \frac{dN}{dM} = \left(\frac{\psi_*}{M_*}\right)\left(\frac{M}{M_*}\right)^\beta \exp\left(-\frac{M}{M_*}\right). \quad (5)$$

We represent the distribution of measurement errors by $p_e(M|M')$, where $p_e(M|M')\ dM$ is the probability that a cluster with a true mass M' has a measured mass in the small interval M to $M + dM$. The predicted observed mass function (ψ_o) is then given by the following integral

$$\psi_{\rm o}(M) = \int_0^\infty p_e(M|M')\ \psi_t(M')\ dM'. \quad (6)$$

For the error-free case, we have $p_e(M|M') = \delta(M - M')$, where δ denotes the usual Dirac delta function, and hence $\psi_{\rm o}(M) = \psi_{\rm t}(M)$, as expected.

The primary error distribution that we adopt is the log-normal distribution:

$$p_e(M|M') = \frac{1}{\sqrt{2\pi}\,\sigma_e M} \exp\left[-\frac{(\ln M - \ln M')^2}{2\sigma_e^2}\right]. \quad (7)$$

Here, σ_e is equal to σ ln 10, where σ is the typical base-10 log uncertainty in the cluster and GMC mass measurements. The predicted observed mass function from Equations (5)–(7) is

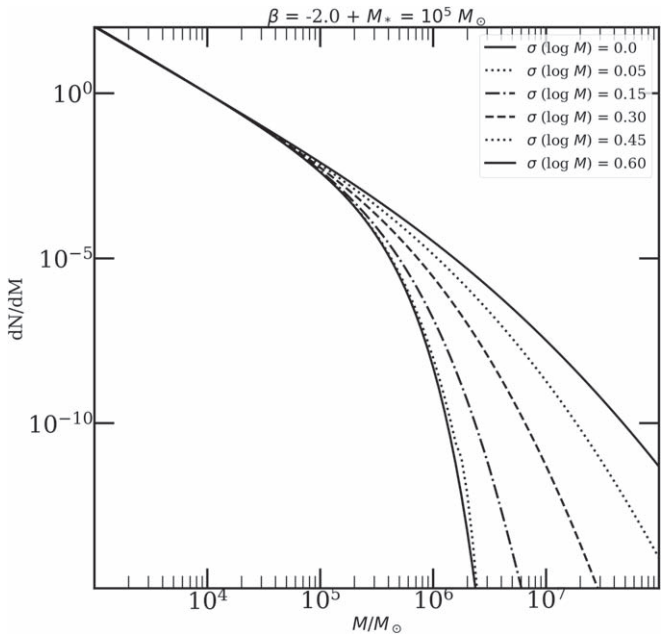

Figure 9. The effect of varying the σ parameter on the shape of the observed mass function (ψ_o) with $\beta = -2$ and $M_* = 10^5\ M_\odot$, where the no-error case is shown as the thick, solid line. Increasing the uncertainty increases the cutoff mass, making the curve appear more and more like a pure power law.

then

$$\psi_o(M) = \frac{1}{\sqrt{2\pi}\,\sigma_e M}\left(\frac{\psi_*}{M_*}\right)\int_0^\infty \left(\frac{M'}{M_*}\right)^\beta \times \exp\left(-\frac{M'}{M_*}\right)\exp\left[-\frac{(\ln M - \ln M')^2}{2\sigma_e^2}\right]dM'. \quad (8)$$

In Figure 9, we show the effect that increasing the uncertainty σ has on the shape of a Schechter function with $\beta = -2.0$ and $M_* = 10^5\ M_\odot$. Larger uncertainties cause the observed mass function (ψ_o) to appear more like a power law, shifting the exponential cutoff to higher masses.

We determine the best-fitting values of β and M_* by comparing ψ_o with the data by the same procedure in both the cases with and without measurement errors, namely, by maximizing the likelihood

$$L(\beta, M_*) = \prod_i P_i, \quad (9)$$

with the probability for the ith cluster given by

$$P_i = \frac{\psi_o(M_i)}{\int_{M_{\min}}^{M_{\max}} \psi(M)\,dM}. \quad (10)$$

While we primarily adopt the log-normal distribution for the measurement uncertainties, we also experimented with a few other functional forms, including simple step functions. We find that these alternative error distributions have less effect on the confidence contours for β and M_* than the log-normal distribution. Thus, we present in Section 4 the two bracketing cases, i.e., the no-error case and the log-normal error case.

Finally, we test our ability to detect an upper mass cutoff for distributions with the same $M_* = 10^5\ M_\odot$, but different power-law indices: $\beta = -1$ (such as for galaxies) versus $\beta = -2$ (such as for clusters and GMCs). The results in Figure 10 are

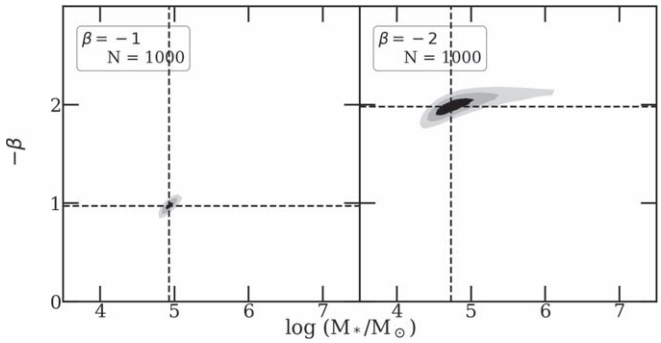

Figure 10. Our maximum-likelihood fitting method applied to mock cluster catalogs. We generate 1000 mock cluster members from an underlying Schechter distribution with $\beta = -1$ (left) and $\beta = -2$ (right), with $M_* = 10^5\ M_\odot$. Note the significantly larger uncertainties in the $\beta = -2$ case, because of the difficulty of measuring a cutoff in steeper distributions.

based on generating 1000 simulated objects from each distribution and performing the maximum-likelihood fitting described on each case. The smaller contours for the $\beta = -1$ case indicate that, for a given sample size, it is easier to detect a physical upper cutoff in populations with shallower power-law indices, such as found for for galaxies. The steeper $\beta \approx -2$ power-law index found for GMC and cluster populations makes the detection of an upper mass cutoff more challenging.

ORCID iDs

Angus Mok https://orcid.org/0000-0001-7413-7534
Rupali Chandar https://orcid.org/0000-0003-0085-4623
S. Michael Fall https://orcid.org/0000-0003-3323-9061

References

Adamo, A., Kruijssen, J. M. D., Bastian, N., Silva-Villa, E., & Ryon, J. 2015, MNRAS, 452, 246
Adamo, A., Ryon, J. E., Messa, M., et al. 2017, ApJ, 841, 131
Akaike, H. 1974, ITAC, 19, 716
Bastian, N., Adamo, A., Gieles, M., et al. 2012, MNRAS, 419, 2606
Baumgardt, H., & Kroupa, P. 2007, MNRAS, 380, 1589
Blitz, L., Fukui, Y., Kawamura, A., et al. 2007, in Protostars and Planets V, ed. B. Reipurth, D. Jewitt, & K. Keil, Vol. 81 (Tucson, AZ: Univ. Arizona Press)
Bolatto, A. D., Wolfire, M., & Leroy, A. K. 2013, ARA&A, 51, 207
Bruzual, G., & Charlot, S. 2003, MNRAS, 344, 1000
Burham, K. P., & Anderson, D. R. 2002, Model Selection and Multimodel Inference (Berlin: Springer)
Calzetti, D., Lee, J. C., Sabbi, E., et al. 2015, AJ, 149, 51
Chabrier, G. 2003, PASP, 115, 763
Chandar, R., Fall, S. M., & Whitmore, B. C. 2015, ApJ, 810, 1
Chandar, R., Fall, S. M., Whitmore, B. C., & Mulia, A. J. 2017, ApJ, 849, 128
Chandar, R., Whitmore, B. C., Dinino, D., et al. 2016, ApJ, 824, 71
Chandar, R., Whitmore, B. C., Kim, H., et al. 2010, ApJ, 719, 966
Colombo, D., Hughes, A., Schinnerer, E., et al. 2014, ApJ, 784, 3
Cook, D. O., Lee, J. C., Adamo, A., et al. 2019, MNRAS, 484, 4897
deGrijs, R., & Anders, P. 2006, MNRAS, 366, 295
Efstathiou, G., Ellis, R. S., & Peterson, B. A. 1988, MNRAS, 232, 431
Elmegreen, B. G., & Falgarone, E. 1996, ApJ, 471, 816
Elson, R. A., & Fall, S. M. 1988, AJ, 96, 1383
Faesi, C. M., Lada, C. J., & Forbrich, J. 2018, ApJ, 857, 19
Fall, S. M., & Chandar, R. 2012, ApJ, 752, 96
Fall, S. M., Chandar, R., & Whitmore, B. C. 2005, ApJL, 631, L133
Fall, S. M., Krumholz, M. R., & Matzner, C. D. 2010, ApJL, 710, L142
Fleck, R. C. J. 1996, ApJ, 458, 739
Freeman, P., Rosolowsky, E., Kruijssen, J. M. D., Bastian, N., & Adamo, A. 2017, MNRAS, 468, 1769
Gieles, M., Portegies Zwart, S. F., Baumgardt, H., et al. 2006, MNRAS, 371, 793

Gratier, P., Braine, J., Rodriguez-Fernandez, N. J., et al. 2012, A&A, 542, A108
Grudić, M. Y., Hopkins, P. F., Faucher-Giguère, C.-A., et al. 2018, MNRAS, 475, 3511
Guszejnov, D., Hopkins, P. F., & Grudić, M. Y. 2018, MNRAS, 477, 5139
Hunter, D. A., Elmegreen, B. G., Dupuy, T. J., & Mortonson, M. 2003, AJ, 126, 1836
Johnson, L. C., Seth, A. C., Dalcanton, J. J., et al. 2017, ApJ, 839, 78
Jordán, A., McLaughlin, D. E., Côté, P., et al. 2007, ApJS, 171, 101
Kim, J.-G., Kim, W.-T., & Ostriker, E. C. 2018, ApJ, 859, 68
Konstantopoulos, I. S., Smith, L. J., Adamo, A., et al. 2013, AJ, 145, 137
Kruijssen, J. M. D. 2014, CQGra, 31, 244006
Krumholz, M. R., McKee, C. F., & Bland-Hawthorn, J. 2019, ARA&A, 57, 227
Larson, R. B. 1981, MNRAS, 194, 809
Leroy, A. K., Walter, F., Bigiel, F., et al. 2009, AJ, 137, 4670
McMullin, J. P., Waters, B., Schiebel, D., Young, W., & Golap, K. 2007, in ASP Conf. Ser. 376, CASA Architecture and Applications, ed. R. A. Shaw, F. Hill, & D. J. Bell (San Francisco, CA: ASP), 127
Messa, M., Adamo, A., Calzetti, D., et al. 2018a, MNRAS, 477, 1683
Messa, M., Adamo, A., Östlin, G., et al. 2018b, MNRAS, 473, 996
Mo, H., van den Bosch, F. C., & White, S. 2010, Galaxy Formation and Evolution (Cambridge: Cambridge Univ. Press)
Mok, A., Chandar, R., & Fall, S. M. 2019, ApJ, 872, 93
Mulia, A. J., Chandar, R., & Whitmore, B. C. 2016, ApJ, 826, 32
Nelder, J. A., & Mead, R. 1965, CompJ, 7, 308
Randriamanakoto, Z., Väisänen, P., Ryder, S., et al. 2013, MNRAS, 431, 554
Rice, T. S., Goodman, A. A., Bergin, E. A., Beaumont, C., & Dame, T. M. 2016, ApJ, 822, 52
Rosolowsky, E. 2005, PASP, 117, 1403
Rosolowsky, E., Keto, E., Matsushita, S., & Willner, S. P. 2007, ApJ, 661, 830
Rosolowsky, E., & Leroy, A. 2006, PASP, 118, 590
Salpeter, E. E. 1955, ApJ, 121, 161
Schechter, P. 1976, ApJ, 203, 297
Schinnerer, E., Meidt, S. E., Pety, J., et al. 2013, ApJ, 779, 42
Sun, J., Leroy, A. K., Schruba, A., et al. 2018, ApJ, 860, 172
Ueda, J., Iono, D., Petitpas, G., et al. 2012, ApJ, 745, 65
Utomo, D., Blitz, L., Davis, T., et al. 2015, ApJ, 803, 16
Wada, K., Spaans, M., & Kim, S. 2000, ApJ, 540, 797
Whitmore, B. C., Chandar, R., & Lee, J. 2020, ApJ, 889, 154
Whitmore, B. C., Chandar, R., Schweizer, F., et al. 2010, AJ, 140, 75
Wong, T., Hughes, A., Ott, J., et al. 2011, ApJS, 197, 16
Wong, T., Hughes, A., Tokuda, K., et al. 2019, ApJ, 885, 50
Wong, T., Ladd, E. F., Brisbin, D., et al. 2008, MNRAS, 386, 1069
Wong, T., Xue, R., Bolatto, A. D., et al. 2013, ApJL, 777, L4
Wu, J., Evans, N. J. I., Shirley, Y. L., & Knez, C. 2010, ApJS, 188, 313
Wu, Y.-L., Sakamoto, K., & Pan, H.-A. 2017, ApJ, 839, 6
Zaragoza-Cardiel, J., Font, J., Beckman, J. E., et al. 2014, MNRAS, 445, 1412
Zhang, Q., & Fall, S. M. 1999, ApJL, 527, L81